Submitted to Journal of Sustainable Cement-Based Materials

Early-age reactivity of calcined kaolinitic clays in LC^3 cements: A multi technique investigation including pair distribution function analysis

Isabel M.R. Bernal; Miguel A.G. Aranda; Isabel Santacruz; Angeles G. De la Torre; Ana Cuesta*

Departamento de Química Inorgánica, Cristalografía y Mineralogía, Universidad de Málaga, Málaga, 29071, Spain.

** email: a_cuesta@uma.es*

Abstract.

Limestone Calcined Clay Cements, LC^3, allows CO_2 emissions savings up to 40%. The resulting binders have competitive mechanical performances after a week. However, the reactivity of LC^3 at early ages is slow and should be improved. Here, we use a multi-technique approach to help in the understanding of early age reactivities which were measured by calorimetry, Frattini assay, and mechanical strengths. The disorder in the kaolinites was quantified by powder diffraction. Some footprints of the local disorder in the resulting metakaolin have been investigated by synchrotron pair distribution function (sPDF). It is concluded that Al-O interatomic correlation position and intensity in the sPDF of the calcined kaolinitic clays could be an additional good descriptor to follow early age reactivity. The results were complemented by ^{27}Al MAS-NMR studies. The rate of the pozzolanic reaction at early ages is governed by the particle size, surface area and local disorder of metakaolin.

Keywords: kaolinitic clays; blended cements; local structure; total scattering; pozzolanic reaction

1. Introduction.

There is great concern about the impact on global warming caused by the production of concrete and consequently, Portland cement (PC), which is its main constituent. The PC industry is a major generator greenhouse gases emissions [1]. Cement manufacturing accounts for ~7% of the anthropogenic CO_2 emissions. A leading work [2] has identified the use of supplementary cementitious materials (SCMs) as the most favorable approach for reducing CO_2 emissions. The use of SCMs is considered today as the strategy with the lowest economic and performance impacts and it is being implemented world-wide. In 2017, the clinker to Portland cement ratio in Europe was 77% [3]. This replacement level should increase to meet the "European Green Deal" but the phase-out of coal fired power plants is already limiting the use of fly ash, just to mention one thread to the current availability of SCMs.

Several authors [4–7] have proposed that LC^3 with clays with a minimum content of ~40 wt% of kaolinite can achieve mechanical performances comparable to those of PC but with a 50 wt% substitution of clinker by calcined clay–limestone [8,9]. The proportions of the mixtures can vary, but the most widely investigated combination contains close to 50 wt% clinker, 30 wt% calcined clay and 15 w% limestone and a minor, optimized, sulfate content. These blends are named as LC^3-50 [8,10]. LC^3-50 can lead to CO_2 emissions reductions close to 40% [9,11]. Moreover, industrial-pilot trials were successfully performed in Cuba and India [8,12]. These materials profit from the pozzolanic effect which is the reaction(s) of silica/alumina-rich precursor, metakaolin, with portlandite, $Ca(OH)_2$, to yield calcium silicate (aluminate) hydrates, C-A-S-H gels, with very good cementing properties as the resulting binders have very dense microstructures [13]. The main drawback of the current proposals for sustainable LC^3-50 cements is their slow hydration kinetics in the first week because the reaction rates of pozzolanic reactions are slower than those of neat PCs.

Natural kaolinitic clays usually have variable amounts of other minerals like feldspars and quartz. Kaolinitic clays mineralogical composition may include the polytypes of the group, kaolinite, nacrite, dickite and halloysite, as well as micas, smectites and chlorites [14]. Kaolinite can be thermally activated between 600ºC and 850ºC by dehydroxylation yielding amorphous metakaolin (MK, $Al_2Si_2O_7$) [7,15,16] which is very reactive and an effective pozzolanic material [17–19]. The activation of clays have been extensively studied [7,20–22]. The optimal activation temperature is related to the degree of ordering of the pristine kaolinite [23]. The transformation that occurs from the crystalline phase to the pozzolanic-active amorphous phase is complicated to follow. Synchrotron powder diffraction jointly with pair distribution function (PDF) is a suitable technique to obtain information about the local scale structure of nanocrystalline/amorphous materials. Moreover, it is possible to distinguish among amorphous, nanocrystalline or crystalline fractions by analyzing total scattering data by PDF methodology. Moreover, information about the local bonding environments can be obtained [24].

The structures of nearly-single phase kaolinites [25–27], and nanostructure information of metakaolin [25,28] and metakaolin-based geopolymers [29,30] have been already studied by PDF. The PDF studies jointly with density functional theory (DFT) modelling revealed that when kaolinite transforms to MK, the Al-O interatomic distance peak changes from a well-defined distribution in kaolinite to a shoulder to the Si-O interatomic distance peak in the calcined specimens [28,29]. This is likely due to the structural re-organization and changes in the coordination of the alumina sites after removing the hydroxyl groups. It was reported that the structure of MK presents aluminum sites mainly in IV and V coordination (with a small percentage of VI-fold) [25,28]. Moreover, it was also found that the environment of aluminum in the layers is the main responsible of the high reactivity of metakaolin [28]. The change in Al-O coordination has been also followed by ^{27}Al magic angle spinning nuclear magnetic resonance (MAS-NMR), using the chemical shifts for Al in tetrahedral (~60 ppm), five-fold (~30 ppm) and octahedral (~5 ppm) coordinations [17,21,31]. The presence of V-coordinated Al indicates a high degree of disorder and loss of crystallinity of the structure [21,31]. It has also been reported that the peak for Al in V-coordination increased with temperature, being the main one at 800ºC. Pozzolanic activity was closely related to the development of five-fold Al species

in the calcined clays [17]. Synchrotron PDF has also been widely used in the cement-related field for understanding the local structures of the complex cement gels, e.g. C-S-H [32–35] and C-A-S-H [36].

The use of calcined kaolinitic clays in PCs is one of the best strategies because MK has demonstrated excellent pozzolanic properties [17,37]. Clays with kaolinite contents above ~40 wt% have been found to be highly pozzolanic after calcination (600-850ºC) [17]. The pozzolanic activity increases with calcination temperature up to a value where recrystallization, and/or agglomeration, starts to play a detrimental role [4]. The positive influence of structural disorder can be partly counterbalanced by the decrease in specific surface area, i.e. the increase in grain size, at higher temperatures that also resulted in blends with better flow features.

The kaolinite content of clays can be determined using a combination between thermal and Rietveld analyses as previously reported [38] and is the main descriptor to follow pozzolanic reactivity. However, other factors can also affect this reactivity, f.i. calcination temperature and time, particle size, dehydroxylation rate, impurity ions within kaolinite, and impurity phases accompanying kaolinite [23,39–42]. Moreover, from a study comparing five kaolinitic clays, it was concluded that clays containing high percentages of kaolinite, ~40 wt% or higher, provide very good pozzolanic activity [43]. Additionally, it was reported that the rate of pozzolanic reaction was enhanced when the kaolinites have more disordered structures. That means that the pozzolanic reactivity is related to the degree of crystallinity of the pristine kaolinite, which can be evaluated by different techniques including XRD [44]. The specific area on the pozzolanic activity has been reported to affect mainly at the very early ages. At longer ages, pozzolanic activity depends mainly on the chemical and mineralogical composition of the clay [42]. There are different methods to test the pozzolanic reactivity of calcined clays, such as Frattini test [45], Chapelle assay [46], calorimetry measurements [5] and activity strength index [16].

The main goal of this work is to contribute to understand the relationship between textural features and local disorder of kaolinitic clays and the early age reactivity of the resulting low carbon cements. This is a previous step before the hydration acceleration of LC^3 binders by admixtures. Here, the reactivities were measured by Frattini essay, isothermal calorimetry and mechanical strength developments. The disorder in the kaolinitic clays was investigated by powder diffraction. Chiefly, some consequences of this local disorder in the resulting calcined clays samples have been investigated by synchrotron pair distribution function. It is noted here that PDF is insensitive to the presence of paramagnetic species that deteriorate the quality of the information derived by ^{27}Al MAS-NMR and that quadrupolar broadening is not an issue. In a nutshell, the rate of the pozzolanic reaction at early ages, seven days or earlier, is governed by the surface area and the local disorder of metakaolin.

2. Materials and Methods.

2.1. Samples.

2.1.1. Kaolinitic clays.

Four clays were employed in this study.

(1) KGa-1b: This is an almost pure commercially-available kaolinite. This clay was purchased from The Clay Minerals Society (USA) and used as reference for tests that require low amounts of sample. To produce high purity MK, KGa-1b was heated at 800ºC for 1h.

(2) FC35-2019: This commercially-available kaolinite-rich clay was provided by Caolines de Vimianzo, S.A.U. (A Coruña, Spain), and will be named hereafter as FC35. The calcination of 20 kgs was performed in the industrial kiln of Inducerama S.L. (a brick-maker company, Malaga, Spain) at 860ºC for 3h. Subsequently, the sample was ground because its resulting $D_{v,50}$, 14.3 μm, was too big. The grinding procedure was performed in a Micro-Deval ball mill (Proeti) at 100 rpm (with 9, 10 and 20 balls of Ø=33, 18 and 10 mm, respectively) in batches of 1.5 kg for 30 minutes. For the PDF study, a small fraction of FC35 clay was heated at 800°C for 1 h.

(3) SY1(A)-2019: This is a commercially-available kaolinite-rich clay provided by Comercial Silices y Caolines de Aragón S.L. (Teruel, Spain); it will be named hereafter as SY1. A large fraction was calcined as described for FC35. After this thermal activation, grinding was not considered necessary as its particle size, $D_{v,50}$, was 10.5 μm.

(4) CVPM3B: This commercially-available kaolinite-rich clay was provided by Arcimusa, S.A. (Zaragoza, Spain) and 20 kgs were also calcined in Inducerama. After calcination, $D_{v,50}$ was 29.1 μm, therefore grinding was required. Firstly, the calcined clay was ground in a Micro-Deval ball mill (Proeti) at 100 rpm, in batches of 1 kg for 1 hour. Secondly, the sample was reground in a ball mill (Proeti) using a 5 L jar at 50 rpm, in batches of 0.5 kg for 1 hour using 3 kg of balls of each size (9.5, 18 and 30 mm diameter).

Table 1 reports selected details about the original clays as well as textural data for the calcined clays after milling. It is explicitly acknowledged that the variation in kaolinite content is not large, i.e. from 83 to 70 wt%. This moderate variation was chosen, for this first study, to avoid the complications arising from a large amount of side phase(s) when dealing with the PDF investigations.

2.1.2. Portland cement, limestone and gypsum.

A commercially available Portland cement, CEM I 42.5R according to EN 197-1 from Financiera y Minera S.A. (Heidelberg Cement Group, Málaga, Spain) was used here. A natural limestone (LS) was selected from one of the quarries in Málaga (Spain) owned by Financiera y Minera S.A. The gypsum used here came from Hormigones y Cementos Andaluces S.L. (Malaga, Spain). The elemental and mineralogical compositions and the textural properties have been reported elsewhere [47].

2.2. Techniques.

2.2.1. Textural characterization. A Mastersizer S (Malvern Panalytical) equipment was used, coupled to a dry chamber (Aero S), to measure the particle size distribution by laser diffraction. The values of the specific surface areas were determined by N_2 adsorption isotherms following the BET (Brunauer–Emmett–Teller) approach with an ASAP 2420 (Micromeritics, USA) instrument. The samples were degassed under vacuum, ~0.2 Pa of pressure, during 24 hours at room temperature, in the same instrument. A Blaine apparatus (Controls) was used to obtain fineness measurements following the EN 196-6 standard. The density of the powders was measured using a helium Pycnometer (Accupyc II 1320 Pycnometer, Micromeritics) equipped with a chamber of 10 cm^3.

2.2.2. X-ray fluorescence analysis (XRF). XRF data were recorded in a PANalytical Axios max system located at the Financiera y Minera cement factory. The samples were prepared in glass beads. For the preparation of these glass beads, 1.4 grams of the powder sample is mixed with 5.6 grams of borate which has a composition of 66.0 wt% $Li_2B_4O_7$ and 34.0 wt% $LiBO_2$. Then, the mixtures were placed into graphite crucibles and introduced on a melting instrument (Claisse-Le Neo Fluxer, Malvern Panalytical).

2.2.3. Laboratory X-ray powder diffraction (LXRPD). All raw clays were characterized in a D8 ADVANCE (Bruker AXS) diffractometer. This equipment (SCAI – Universidad de Málaga) contains a Johansson monochromator which provides monochromatic Mo-Kα_1 radiation (λ=0.7093 Å). The measurements were carried out in transmission geometry (θ/θ). Samples were spun during data collection. An internal standard, ~15 wt% of α-Al_2O_3 (AlfaAesar), was added to calcined clays to quantify the ACn (amorphous and non-determined crystalline) content [48]. LXRPD data, for the calcined clays mixed with the standard, were recorded in reflection mode using a PANalytical diffractometer, X'Pert MPD PRO model (SCAI – Universidad de Málaga). This diffractometer is equipped with a Ge (111) primary Johansson monochromator that yields monochromatic CuKα_1 radiation (λ=1.54059 Å). It also has a X'Celerator detector, working in scanning mode with maximum active length. Samples were also spun during data collection.

To obtain the Rietveld analyses, GSAS software package was used [49]. The refined overall parameters were: background coefficients, zero-shift error, cell parameters, and peak shape parameters using a pseudo-Voigt peak shape function.

2.2.4. Total Scattering Synchrotron X-ray powder diffraction (SXRPD). Selected samples were analyzed by total scattering SXRPD. The BL04-MSPD beamline at ALBA synchrotron (Barcelona, Spain) was employed to collect the patterns in Debye-Scherrer (transmission) mode [50]. Si640d NIST standard (a=5.43123 Å) was used to determine the resulting wavelength, 0.41362(1) Å. The final dataset is the result of merging four patterns (~40 min) for each sample, in the very wide angular range, 1 to 130° (2θ).

PDF data were obtained with PDFgetX3 software [51] by applying Q_{max}=21 $Å^{-1}$. The data analysis was performed with PDFGui software [52]. The instrumental parameters, Qdamp=0.027 $Å^{-1}$ and Qbroad=0.089 $Å^{-1}$, were obtained by using crystalline nickel. The optimized parameters were: scale factors, unit cell values and atomic displacement parameters (ADPs), including the delta2 value, low-r correlated motion peak sharpening factor [53,54], when analyzing the low-r region.

2.2.5. Thermal analysis (TA). An SDT-Q600 analyzer from TA instruments (New Castle, DE) was employed. The temperature was raised to 1000°C at a rate of 10°C/min. Open platinum crucibles were used, under synthetic air flow of 100 ml/min.

2.2.6. ^{27}Al magic angle spinning nuclear magnetic resonance (MAS-NMR). A Bruker AXS - AVIII HD 600 NMR spectrometer (14.1 T of magnetic field) at 156.37 MHz using a 2.5 mm triple-resonance DVT probe was used to record the ^{27}Al spectra at RT with a spinning rate of 20 kHz. The ^{27}Al MAS-NMR spectra were acquired by applying an excitation pulse of 0.29 μs and 1 s delay without ^{1}H decoupling and summing up 2000 scans. Data are referenced to the chemical shift of a 1 M solution of $Al(NO_3)_3$.

2.2.7. Isothermal calorimetry. These measurements were carried out in a Thermal Activity Monitor (TAM) instrument. The solids were mixed with water, by hand, outside the calorimeter for 1 min, and after that, with a vortex mixer, for another minute. The resulting pastes were poured into glass ampoules. The heat flow data were collected up to 6 days at 40ºC to determine the pozzolanic activity [5]; for temperature stabilization, the measurement started after 45 minutes since mixing. The measurements were carried out in a simplified system using portlandite, calcined clays and limestone, following all final recommendations [5]. Thus, the mass ratios were: portlandite/calcined clay=3.0, LS/calcined clay=0.50, water/binder=1.20, K_2SO_4/calcined clay=0.117 and KOH/calcined clay=0.025.

2.2.8. Frattini test. This test is performed by pouring 100 ml of distilled water into a polyethylene container and placing it into a water bath at 40ºC until thermal equilibrium. Then, the container is removed and 20 g of sample were added. The samples here were a mixture of 75 wt% of PC42.5R and 25 wt% of the calcined clay. The container was immediately closed, the mixture was stirred for a few seconds to avoid lump formation and the system was placed back in the water bath. After a period of 7 days, the container was removed and then, the solution was filtered at RT using a low porosity double filter paper (2 μm). The hydroxide concentration, $[OH^-]$, was determined using a solution of HCl (0.1 N) to carry out the titration, where a methyl orange solution was employed as indicator. To determine the concentration of calcium ions, $[Ca^{2+}]$, the pH was fixed to 12.5 by using a 10 wt% NaOH solution. Then, the titration was carried out using 0.03 mol/L of ethylenediaminetetra acetic acid (EDTA) solution and murexide as indicator for photometric determination. The results are presented in a graph where the concentration of Ca^{2+} is expressed as equivalent CaO, in mmol/L, on the y-axis, versus concentration of hydroxide ions, $[OH^-]$, in mmol/L, on the x-axis. In addition, the theoretical $Ca(OH)_2$ solubility curve is also plotted as described in the EN 196-5 standard. Pozzolanic activity is reflected in the experimental results where the data are located below the $Ca(OH)_2$ solubility curve indicating a portlandite consumption.

2.2.9. Compressive strength. Mortars were fabricated following EN 196-1 standard. The LC^3 systems contained 52 wt% of PC42.5R, 30 wt% of calcined clay, 15 wt% of limestone and 3 wt% of additional gypsum. All mortars were prepared at binder/sand and water/binder mass ratios of 1/3 and 0.40, respectively. LC^3 mortars were prepared with 0.4 wt% (active matter referred to the blend) of a polycarboxylate based superplasticizer (Floadis 1623, with 25 wt% of active matter). Mortars were cast and then de-aired in a jolting table (Ibertest, model IB-32-0 45E, 2002) as indicated in the standard. The prisms, 40×40×160 mm^3, were kept at 20ºC and 99% RH for 24 hours. Subsequently, they were unmolded and cured in tap water at T=20ºC until testing. Mechanical strengths of mortars were measured in a press (Model Autotest 200/10 W, Ibertest, Madrid, Spain) at a constant loading rate of 1.5 $MPa \cdot s^{-1}$. The compressive values (average of six measurements) are reported at 2, 7 and 28 days of hydration.

3. Results and Discussion

3.1. Initial characterization of kaolinitic clays.

The textural properties are very important to understand the reactivity of each calcined clay. Thus, a thorough textural characterization was carried out for the employed calcined clays. Air permeabilities (Blaine values), BET surface areas and PSDs were measured and the values are gathered in Table 1. The PSD curves are shown in Figure S1. Moreover, the density values are also included. The elemental analyses for the calcined clays were also measured and the data are reported in Table S1.

The disorder of the kaolinite phases was measured by using the Aparicio-Galan-Ferrell index (AGFI) [55]. Peak deconvolution was performed between 8.7 and 11.9º (2θ) by least-squares fitting using the program Origin 2018. The symmetrical Pearson VII function was chosen according to the reported methodology [38]. Firstly, the background was subtracted from the whole pattern and secondly, peak position, height, shape and full width at half maximum (FWHM) values were refined. Tables 1 and S2 show the AGFI indexes and FWHM values for (020), ($1\bar{1}0$) and ($11\bar{1}$) kaolinite reflections. The peak deconvolutions of the powder patterns for KGa-1b and CVPM3B clays are displayed in Figure 1. Figure S2 shows the peak deconvolution for all the raw clays. According to the derived AGFI values, FC35, SY1 and CVPM3B clays can be considered as high-defect kaolinites [55].

Table 1. Key characterization data for the pristine* and calcined# clays.

Clays	KGa-1b	FC35	SY1	CVPM3B
Kaolinite content /wt%	95	83	74	70
AGFI	1.09	0.49	0.58	0.54
FWHM (001) / º	0.11(1)	0.14(1)	0.17(1)	0.31(1)
Milling details for the calcined clay$	No milling	Micro-Deval ball mill (30 minutes)	No milling	Micro-Deval ball mill (1 hour) + standard ball mill (1 hour)
ρ /g/cm^3	2.605	2.606	2.619	2.747
$D_{v,10}$ /μm	0.7	1.8	2.2	0.8
$D_{v,50}$ /μm	2.3	11.1	10.5	5.8
$D_{v,90}$ /μm	24.5	42.4	39.7	55.0
Blaine /m^2/kg	1000	467	431	1280
BET surface area /m^2/g	11.3(1)	9.6(1)	9.1(1)	23.7(1)

* For the raw clays, the kaolinite content, the AGFI values and the FWHM of (001) diffraction peaks are given to characterize the kaolinite phase including the degree of disorder before calcination.

Textural properties of these calcined clays specimens are also reported: density, particle size distribution, Blaine air permeabilities and BET specific surface area.

$ Milling conditions employed for conditioning the calcined clays.

Another characterization of the degree of crystallinity of the kaolinite phases can be obtained by measuring and comparing the full width at half maximum (FWHM) of the first diffraction peak (001) which is not overlapped. These values are summarized in Tables 1 and S3. The reference kaolinite sample displayed the narrowest FWHM value. SY1 and FC35 showed similar widths. Finally, the FWHM value for CVPM3B was much higher, which indicates a larger degree of disorder in the packing of their layers.

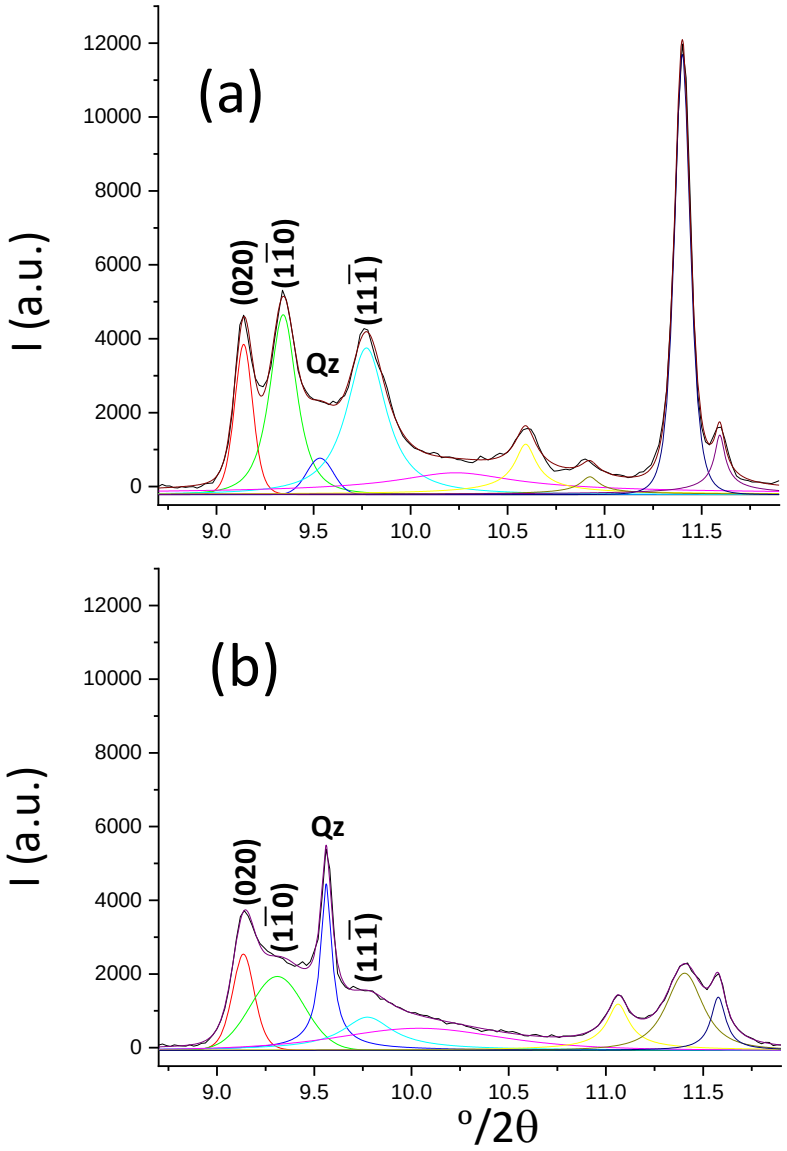

Figure 1. Peak deconvolution of a selected range of the powder pattern, Mo $K\alpha_1$, for (a) KGa-1b and (b) CVPM3B samples. The outputs are used for the calculation of AGFI. The Miller indexes of the kaolinite diffraction peaks are labelled.

Since the particle size of CVPM3B was smaller than those of FC35 and SY1, see Table 1, alternative milling conditions were employed, in small portions, for the pristine calcined clays (~15 g) to achieve comparable pozzolanic early-age reactivities. Table 2 gives the PSDs, BET specific surface area and Blaine air permeability values of the additional calcined clays specifically prepared for the Frattini and calorimetric assays.

Table 2. Milling conditions and textural properties for the additional calcined clay specimens.

Calcined clays	FC35-b	SY1-b	CVPM3B-b
Milling conditions	Micro-Deval ball mill (30 minutes) + disc mill (30 seconds)	Disc mill (30 seconds)	Micro-Deval ball mill (1 hour) + disc mill (60 seconds)
$D_{v,10}$ /μm	0.8	0.4	0.9
$D_{v,50}$ /μm	5.1	4.9	10.6
$D_{v,90}$ /μm	21.6	19.7	146.0
Blaine /m^2/kg	930	826	1184
BET surface area /m^2/g	11.8(1)	12.3(1)	23.5(1)

3.2. Kaolinite content determination by TA and Rietveld analysis.

The kaolinite contents in the raw clays were determined by TA and LXRPD using Rietveld method. Both approaches should provide similar results within the uncertainties of the methodologies. Figure 2 and Figures S3-S5 display the thermal analysis traces for all the raw clays. The kaolinite contents derived from thermal analysis were determined using the tangential method [56], and the results are reported in Table 3. This methodology has been previously used for the quantification of kaolinite as the influence of other clays (illite/muscovite) in the quantification is minimized [38,57].

Table 3. Kaolinite contents calculated by three methods (Rietveld, thermal analysis and XRF), all data in wt%.

Clay	Kaolinite content / Rietveld	Kaolinite content / thermal analysis loss – composition	Kaolinite content / XRF - Al_2O_3 – composition	Estimated kaolinite content
Kaolinite–theoretical[*]	*100*	*13.95 – 100*	*39.51 – 100*	*100%*
KGa-1b	98	12.7 – 91.0	8.3 – 96.9	95%
FC35	85	10.1 – 72.4	35.8 – 90.6	83%
SY1	76	8.8 – 63.1	32.4 – 82.0	74%
CVPM3B	78	8.6 – 61.6	27.7 – 70.1	70%

[*] The theoretical values for single phase (stoichiometric) kaolinite are given in italics as reference.

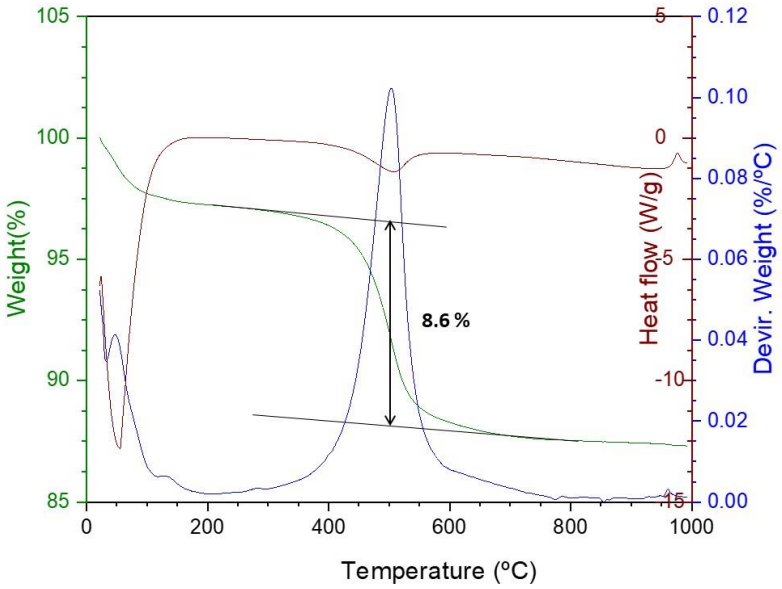

Figure 2. Thermal analysis curves of raw CVPM3B clay, showing the dehydroxylation range. Green, blue and brown traces indicate the weight loss, the derivative of the weight loss, and heat flow, respectively. The weight loss between 400-650ºC, determined a kaolinite content of ~62 wt%.

Moreover, quantitative phase analyses (RQPA) of the raw clays have been obtained by analyzing the LXRPD data, see Table S4. The almost-pure kaolinite clay, KGa-1b, also includes small amounts of anatase (1.9 wt%) and rutile (0.4 wt%). FC35 contains kaolinite, muscovite and quartz; SY1 has kaolinite, muscovite, microcline and quartz; and finally, CVPM3B contains kaolinite, quartz and iron oxide. Preferred orientation effect was observed for kaolinite phase along (001) axis and it was corrected using the March-Dollase algorithm [58]. The Rietveld plot for CVPM3B, as an example, is displayed in Figure 3 and the Rietveld plots for the other clays are deposited in the Supplementary Information, Figs S6-S8. The resulting kaolinite contents obtained by Rietveld analysis are also given in Table 3. The Rietveld quantification method is not fully accurate for highly disordered phases due to the difficulties with fitting the patterns containing broad diffraction peaks. Moreover, if internal standard is not added, the presence of amorphous/nanocrystalline components also contributes to the uncertainties. Hence, it setups an upper limit. Thermal data are also subjected to errors due to the possible overlapping of weight losses from other phases in the computed temperature range. Finally, the Al_2O_3 content is also approximated as there are other aluminum containing minerals in minor quantities. Taken all together, approximate average kaolinite contents can be determined for each clay, see right column in Table 3. It must be noted that, as expected to minimize the possible contributions from other clays, the tangential method in TA (slightly) underestimates the kaolinite contents for all the samples.

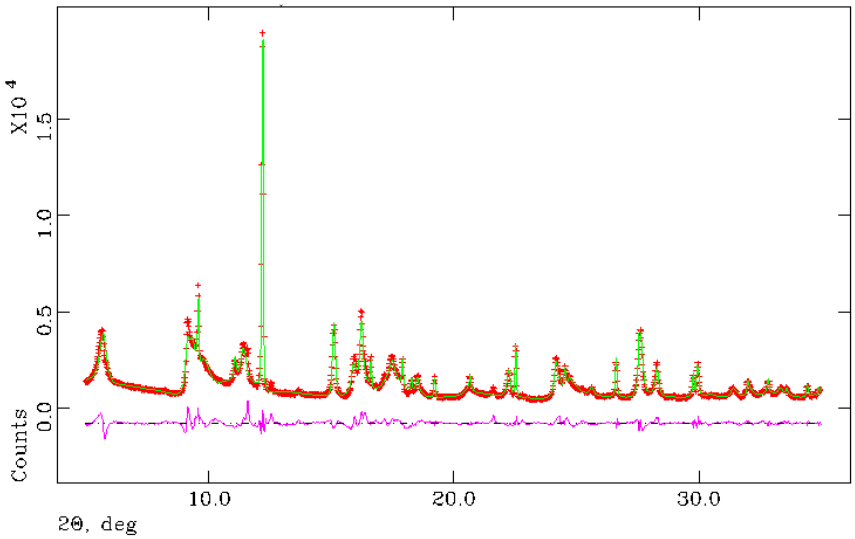

Figure 3. Rietveld plots for the raw CVPM3B clay (Mo-Kα_1 monochromatic radiation, λ=0.71 Å), yielding the following crystalline phase composition: 78 wt% of kaolinite, 14 wt% of quartz, and 8 wt% of iron oxide. The kaolinite content is likely (slightly) lower because some additional (low intensity) diffraction peaks were not accounted for.

3.3. Amorphous content determination in the calcined clays by Rietveld analysis.

Calcined clays were mixed with 15 wt% of α-Al_2O_3 used as internal standard. The raw LXRPD patterns are displayed in Figure 4 where the main diffraction peaks are labelled. The kaolinite reflections have disappeared in the LXRPD patterns of the calcined clays due to the formation of amorphous metakaolin. The main reflections of the other components/clays such as muscovite and microcline are still visible after the calcination temperature of 860ºC.

RQPA results including the ACn values are summarized in Table S5. The four Rietveld plots with the final fits are deposited in the Supplementary Information as Figures S9-S12. On the one hand, it is shown that the ACn content for the calcined reference clay, KGa-1b, was the highest, 98 wt% in agreement with its kaolinite content given in Table 3. It can be considered that all this amorphous material is MK. On the other hand, the overall amorphous contents for the three calcined clays were very similar ranging from 76-77 wt%. However, this does not necessarily mean that these amounts are MK. For calcined FC35, the initial kaolinite content, ~83 wt%, should lead to 71.4 g of MK and 17 g of the remaining phases. A renormalization to 100%, under the assumption that the

remaining phases do not loss water, the resulting MK content should be 81 wt%. There is a relative good agreement with the measured value, 77 wt%, indicating that most, if not all, the amorphous content is MK for this sample. However, this simple calculation, for calcined SY1 and CVPM3B, resulted in expected values for the MK content of 71 and 66 wt%, respectively. This seems to indicate that there is an additional amorphous phase ranging 5-10 wt% for these two samples.

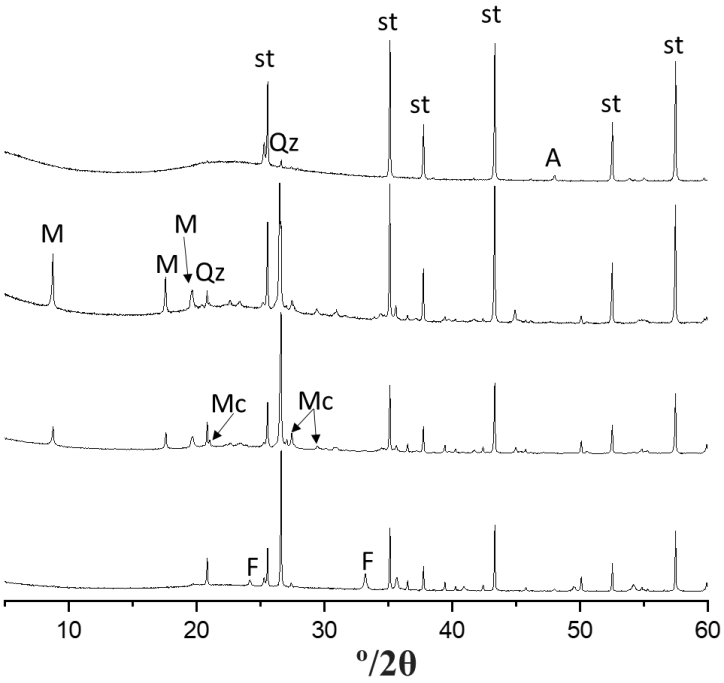

Figure 4. Laboratory X-ray powder diffraction patterns, CuKα_1, λ=1.54 Å, for the calcined clays with the internal standard; from top to bottom: KGa-1b, FC35, SY1, CVPM3B. The main peaks are labelled following the notation: internal standard (st), muscovite (M), quartz (Qz), anatase (A), Microcline (Mc) and F (iron oxide). The hump at ~23º/2θ, typical of MK, is evident in all patterns.

3.4. ^{27}Al MAS-NMR in raw and calcined clays.

^{27}Al MAS-NMR spectra were collected for all raw and calcined clays, see Figure 5. The ^{27}Al MAS-NMR spectra for the KGa-1b, FC35 and CVPM3B raw clays show a single sharp resonance close to 5.0 ppm due to octahedrally coordinated aluminum in agreement with many previous publications [21,59,60]. The SY1 clay also shows two small bands located at 57.5 and 71.5 ppm that are due to aluminum in tetrahedral coordinations. These bands were reported to be related to fully condensed Al(OSi)$_4$ sites (at 56-59 ppm) and to Al sites in layered clay mineral structures (at 70-71 ppm) [17,21].

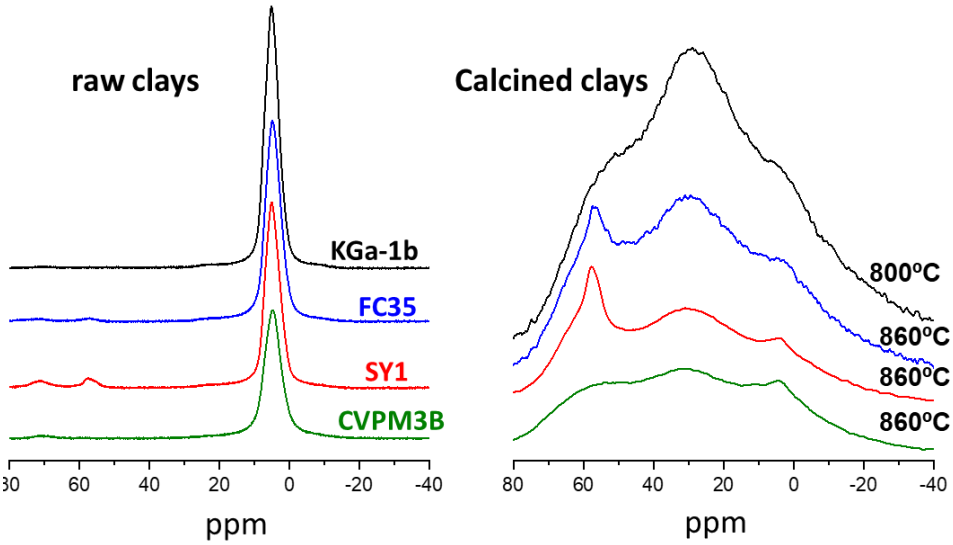

Figure 5. ^{27}Al MAS-NMR spectra for the studied clays, (left) raw clays and (right) calcined clays.

As expected, the ^{27}Al MAS-NMR spectra for the calcined clays show the changes in the aluminum environments upon heating. For the reference KGa-1b clay, there are three broad and severely overlapped bands at 55, 30 and 5 ppm, which are due to aluminums in tetrahedral, fivefold and octahedral coordinations, respectively [17,21]. The large line-broadening is due to its amorphous structure and the effects of the second-order quadrupolar interactions, which may affect the peaks in different ways. Thus, it is difficult to estimate relative fractions of the different coordination states from the reported spectra. In any case, the three calcined clays show very broad resonances centered at ~30 ppm which are due to fivefold aluminum environments. In addition, FC35 and SY1 calcined clays spectra show sharper resonances close to 57 ppm, which are due to tetrahedral aluminum coordination from the aluminum-containing impurities of these calcined clays, see Table S5. The ^{27}Al MAS-NMR spectrum for calcined CVPM3B is more similar to that of reference MK and it shows three resonance broad bands located at 57, 30 and 4 ppm. It should be noted that the fivefold Al sites have been reported to be the most reactive Al-sites in MK samples [31,61].

3.5. PDF studies in kaolinite and calcined clays.

The total scattering SXRPD raw data for the reference kaolinite sample and the four studied calcined clays are plotted in Figure 6. In addition to the sharp peaks corresponding to the crystalline phases, the oscillations due to the (amorphous) MK component are also visible in the calcined clay traces.

The PDF data for the reference kaolinite was fitted in two different ranges. Firstly, the low r-range between 1.4–10 Å was refined and R_W converged to 22.3 %. The unit cell parameters were a=5.172 Å, b=8.919 Å, c=7.382 Å, α=92.2º β=104.1º and γ=90.1º and the optimized ADPs converged to 0.0022, 0.0038 and 0.0124 Å^2 for Al, Si, O, respectively. Figure 7 shows the PDF fit of this low r-region which also includes the contribution of the different atom-atom interatomic distances from the final structure. The first average Si-O interatomic distance of the SiO_4 groups converged to 1.62 Å which is identical to that previously reported [26], and slightly smaller than 1.64 Å reported in [27]. The first average Al-O interatomic distance of the AlO_6 groups was 1.94 Å which is slightly larger than that reported in [26], 1.91 Å, and very close to the value reported in [27], 1.95 Å. The different inter atomic correlations for this well described structure are given to help in the understanding of the MK structural features, see just below. Moreover, a full PDF fit was performed in a larger range of 1.4 – 40 Å and the R_W was 29.9 %. For this fit, the unit cell values converged to a=5.157 Å, b=8.946 Å, c=7.405 Å, α=91.5 º β=104.9º and γ=89.9º and ADPs were 0.0038, 0.0053 and 0.0161 Å^2 for Al, Si, O, respectively. The PDF fit in, the r-range of 10–40 Å, is displayed in Figure 8. The good agreement over the large r-range shows that this structure captures the fine details of this kaolinite.

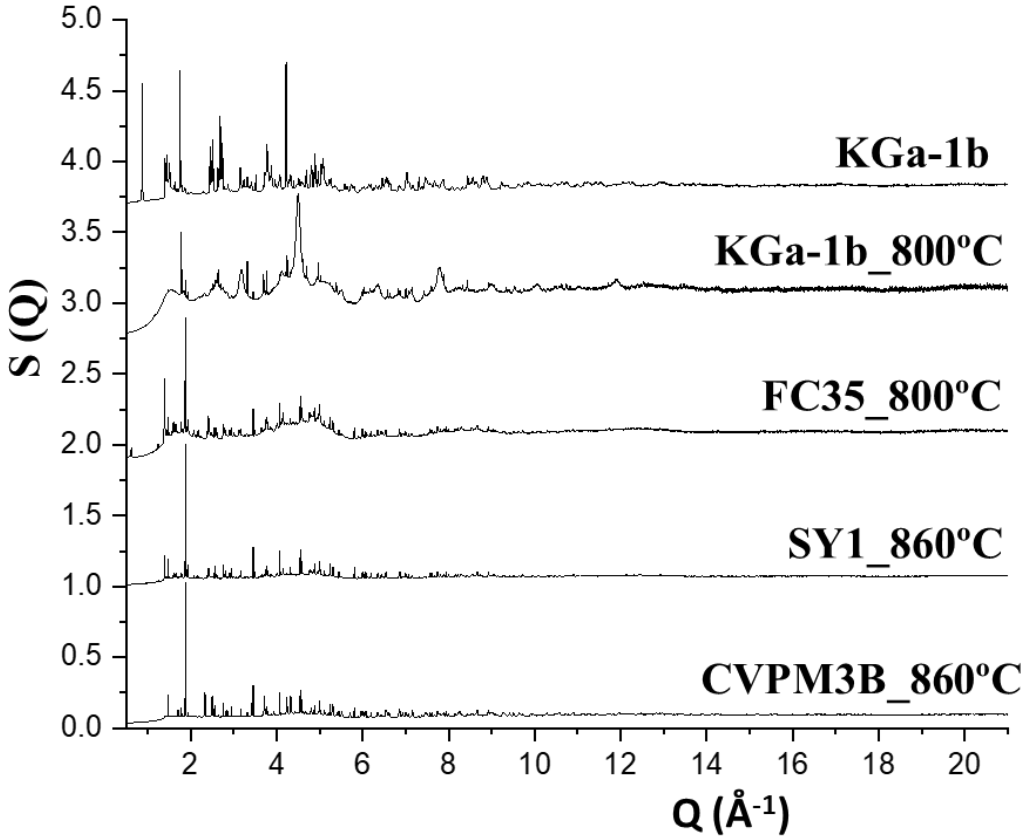

Figure 6. Synchrotron X-ray total scattering functions, S(Q), for the clays. The patterns have been normalized respect to their highest diffraction peak and vertically displaced for adequate visualization.

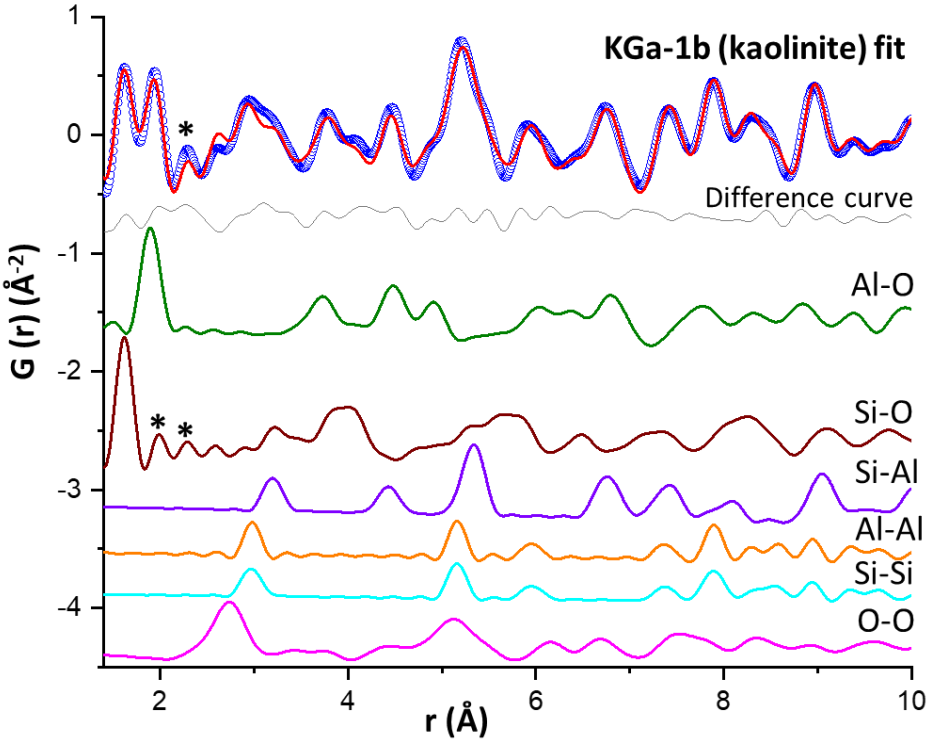

Figure 7. Experimental (blue circles) and fitted (red solid line) PDF patterns for kaolinite, KGa-1b sample, in the low r-region. Difference curve is shown as grey line. The individual contributions (from the refined local structure) for the different atom–atom distances are also displayed in different colors. Ripples (not interatomic correlations) are marked with stars for better understanding.

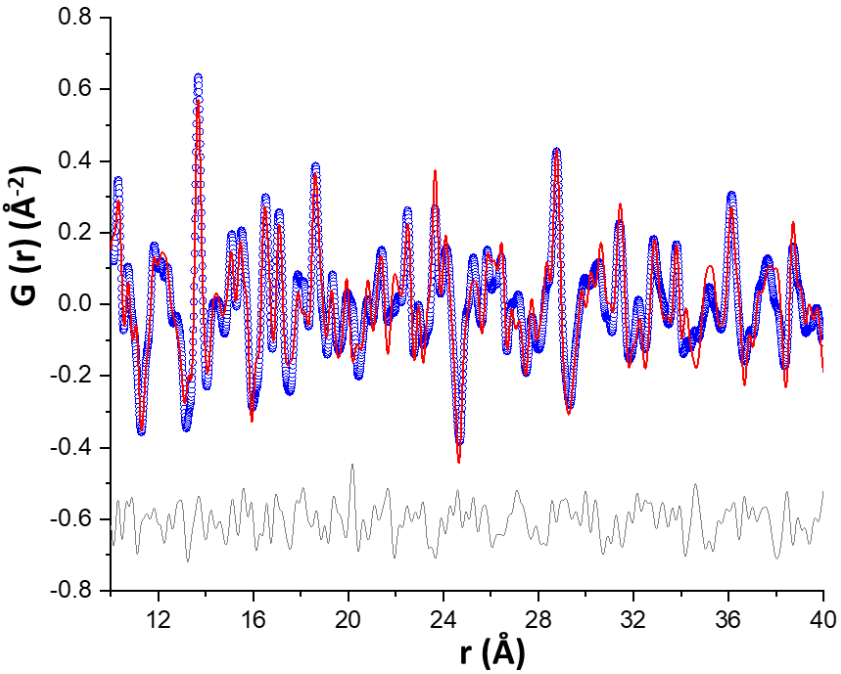

Figure 8. Experimental (blue circles) and fitted (red solid line) PDF patterns for kaolinite in the high r-region. Difference curve is shown as a grey line at the bottom of the panel.

Raw PDF patterns for the reference kaolinite and the calcined clays in the range 1.0–10 Å are shown in Figure 9(a). The analysis and discussion of these data have to be exercised with care as the commercial calcined clays contain variable amounts of crystalline phases that can mask the contribution of MK. Even for calcined KGa-1b, which has about 95 wt% of MK, the contribution of the remaining crystalline phases is not negligible. The calcined samples show low structural order. Because these two features, the low order in the MK structure and the presence of crystalline impurity phases, the discussion is restricted to structural features smaller than 6 Å, see Figure 9(b), where the contribution of (nearly amorphous) MK is relatively larger.

The first PDF peak, which corresponds to the Si(IV)-O interatomic distance, is located at 1.62 Å for kaolinite and the reference MK. The position of this peak does not present important variations after calcination, i.e. kaolinite dehydroxylation. Its intensity (integrated area) can slightly increase as it may incorporate any Al(IV)-O structural correlation in the calcined phases. Conversely, the PDF peak corresponding to the Al-O interatomic distance located at 1.94 Å for kaolinite, Al(VI)-O, undergoes very significant changes on heating, see Figure 9(b). A first qualitative study will be followed by a quantitative one. Figure 9(b) shows that, as expected because the dehydroxylation is carried out within the aluminum layers, the structural correlations that change the most all involve aluminum. The Al-O distance correlation at ~1.94 Å involves Al(V)-O and Al(VI)-O from MK and other aluminosilicates. The integrated area decreases on heating as a fraction of the aluminates changes to tetrahedral coordination. Furthermore, the Al···Al correlations at ~3.0 and 5.2 Å, also undergo strong variations. These modifications are fully in line with previous PDF investigations studying the calcination of kaolinite [25,27,28].

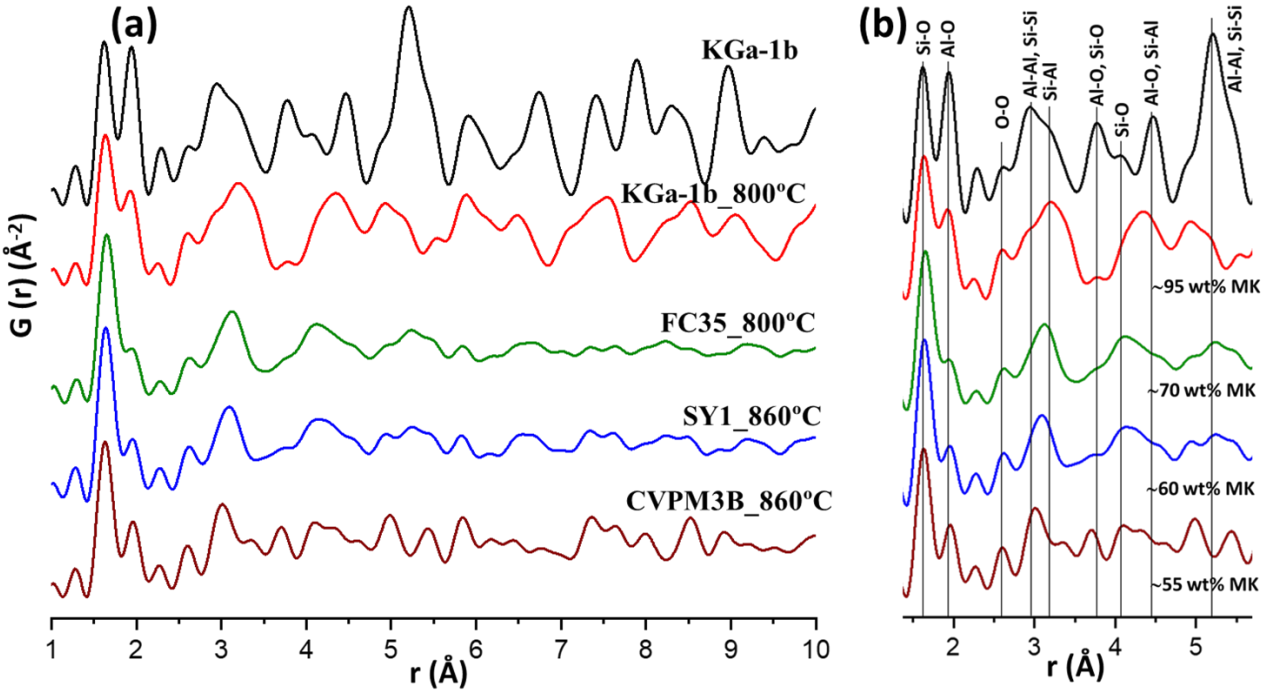

Figure 9. Experimental synchrotron PDF patterns for the different studied clays (a) from 1 to 10 Å; and (b) selected range, from 1.5 to 5.5 Å, with the main interatomic correlations highlighted. The approximate MK contents are stated assuming complete transformation from kaolinite to MK.

The original contribution of this work is twofold: i) the quantitative study which has been focused on the peak deconvolution for the Si(IV)-O and Al(V,VI)-O interatomic distances in the 1.40 – 2.15 Å r-range, and ii) the study of a series with variable amount of kaolinite and local disorder within the kaolinite structure. The results of this quantitative study are summarized in Table 4 and the fits are displayed in Figure 10. Firstly, for kaolinite, the ratio of integrated areas of the Al(VI)-O and Si(IV)-O bands is 0.95, see Table 3. The Al:Si molar ratio of kaolinite is 1:1, and the Al:Si elemental ratio deduced from the XRF analysis of the studied specimen is 1.03. The agreement between these values shows the good accuracy of the study. Furthermore, the calculated Si(IV)-O and Al(VI)-O distances based on the Shannon radii are 1.66 and 1.935 Å, respectively. The agreement between the interatomic distances in kaolinite, see Table 4, and the Shannon's derived ones indicate that this structure is not significantly strained. Secondly, in the kaolinite to MK transition, the Si-O interatomic distance changes from 1.62 to 1.63 and the Al-O one from 1.94 to 1.92 Å. The (minor) shortening of the Al-O bond distances are due to the change in Al coordination environment from octahedral to fivefold, see the ^{27}Al MAS-NMR results above. This shortening of Al-O has been predicted by DFT calculations in MK, see Figure 5 of [28], but there is not quantitative agreement. At this stage it should be noted that the Shannon's derived Al(V)-O distance is 1.88 Å. The larger Al(V)-O distances in MK is very likely a signature of the strains within this complex (amorphous) structure. Thirdly and chiefly, the ratios of the Al-O/Si-O integrated areas decrease strongly in MK although the Al/Si molar ratio is maintained. This has been qualitatively reported before, [25,27,28], but it remained unexplained. We justify this because any Al(IV)-O contribution in the calcined clays are overlapped with the Si-O band resulting in an enhanced ratio. On the other hand, for the calcined clays, the Al-O distance at ~1.94 Å contains the contributions of Al(V)-O and Al(VI)-O interatomic correlations. In order to support this, the Al/Si elemental ratios derived from the XRF analyses are also given in Table 4. Importantly, the Al/Si elemental ratio for CVPM3B, i.e. 0.71, is smaller than those for FC35 and SY1. However, the Al(V)-O/Si-O area ratio, 0.38 see Table 4, is higher than the corresponding values for FC35 and SY1, 0.30 and 0.28, respectively. This could be due to a larger contribution of highly-strained AlO_4 groups in CVPM3B calcined clay, which is also seen in the ^{27}Al

MAS-NMR study, see Figure 5. Finally, it should be noted that the average Al-O distance for calcined CVPM3B is 1.95 Å. This value is very high for the main Al(V)-O bond distances in MK and it is likely a signature of the higher disorder in the original kaolinite.

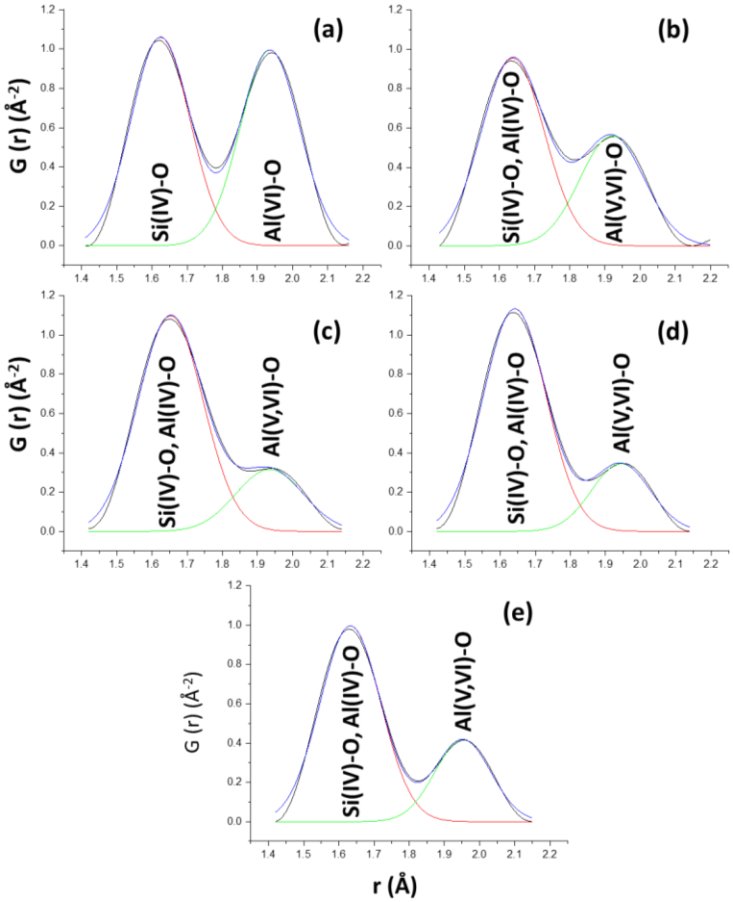

Figure 10. Peak deconvolution for the Si-O and Al-O interatomic distances for (a) raw kaolinite KGa-1b, (b) calcined KGa-1b (MK), (c) calcined FC35, (d) calcined SY1 and (e) calcined CVPM3B.

Table 4. Peak positions and areas of the Al-O and Si-O interatomic distance peaks for the raw kaolinite and the calcined clays from PDF analyses.

Clays	Si-O position/Å	Si-O area	Si-O FWHM/Å	Al-O position/Å	Al-O area	Al-O FWHM/Å	Al-O/Si-O area ratio	Al/Si ratio[#]
KGa-1b	1.62	0.222	0.20	1.94	0.210	0.20	0.95	1.03
KGa-1b[*]	1.63	0.216	0.21	1.92	0.129	0.22	0.60	1.03
FC35[*]	1.65	0.255	0.22	1.93	0.076	0.23	0.30	0.91
SY1[*]	1.64	0.256	0.21	1.94	0.072	0.20	0.28	0.75
CVPM3B[*]	1.63	0.216	0.20	1.95	0.083	0.19	0.38	0.71

[*]Calcined clays. [#] Al/Si elemental ratio derived from the XRF analyses.

The pozzolanic early-age reactivity depends upon a number of variables, the most important ones being MK content, small particle sizes, large specific surface areas and higher disorder. PDF analyses cannot quantify the particle sizes. However, this type of study can determine the relative amount of MK by following the integrated area of the Al(V)-O structural correlation. Furthermore, the average position of that correlation, close to 1.93 Å, gives indication of the strain/disorder of the MK, with larger values mapping higher disorder.

3.6. Frattini test and calorimetry for LC³ binders.

Frattini tests were carried out for all calcined clays using a mixture of 75 wt% of PC-42.5R and 25 wt% of calcined clay, to compare their pozzolanic activities [62,63]. Figure 11 and Table S6 display

the Frattini results. As expected, the pozzolanic activity for calcined KGa-1b is the highest due to its higher MK content and small particle size, see Table 1. It can also be seen that pozzolanic activities for the calcined clays with lower particle sizes, $D_{v,50}$ ~5 μm, are larger than those derived for clays with $D_{v,50}$ ~10 μm. The average reduction of [CaO] decreases from 87% to 65 % when the average particle size increases from 5 to 10 μm. As the kaolinite content and the disorder of the clay are intrinsic properties, the milling procedure provides a valuable degree of freedom in order to boost early age reactivities, if/when needed. These results are in line with previous publications [38,39,43].

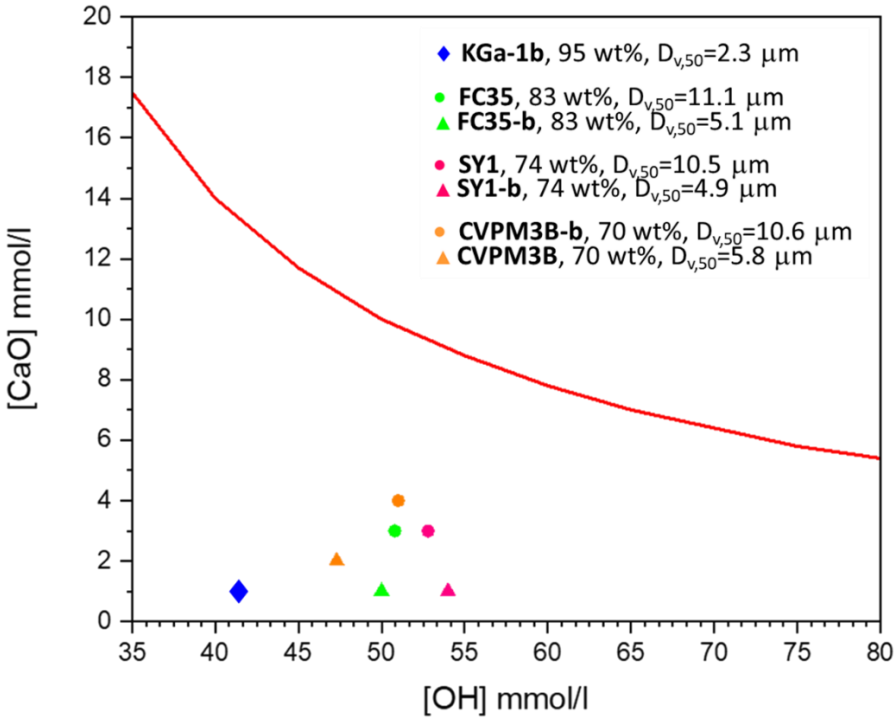

Figure 11. Frattini test results for calcined clays using EN195-5 standard to determine the theoretical maximum amount of [CaO] (red line) after seven days. The average particle sizes of the studied calcined clays are explicitly stated.

Calorimetry experiments were also carried out at 40ºC to further characterize the pozzolanic activities of all calcined clays. Figure 12a displays the cumulative heats, up to 140 hours, developed by the different calcined clays referred to 1 gram of solid, i.e. calcined clay plus LS and $Ca(OH)_2$, see experimental. At the final reaction time, the released heat by KGa-1b was 235 J/g. This high value is a combination of its MK content (the highest) and its particle size (the smallest). The corresponding values for FC35 were 196 and 168 J/g for the samples milled to 5 and 11 μm, respectively. The difference for SY-1 was much smaller, the values being 160 and 158 J/g for the specimens milled to 5 and 10 μm, respectively. For CVPM3B, the clay with the lowest MK content, the heat release was smaller and the corresponding values were 148 and 133 J/g. As expected, the overall released heat correlates well with the MK content. This relationship is much clearer for the samples with $D_{v,50}$~5 μm than for those milled to $D_{v,50}$~10 μm. This is expected because for smaller particle sizes, the surfaces are larger and the kinetics effects play a smaller role.

This work focuses on the reactivity at early ages. Therefore, Figure 12b displays the heat flow traces for the studied samples up to 24 hours. At this time, kinetic factors are more important. For instance, this is shown up by CVPM3B, the clay with the lowest kaolinite content but having the largest disorder. It can be seen that this calcined clay milled down to 6 μm, released more heat than SY-1 milled to a similar size and nearly the same of FC35 in spite that this sample has about 15 wt% higher kaolinite content. Thus, it is becoming evident that the local disorder of kaolinites accelerates the pozzolanic reaction at early ages and it could account for some scattering in early age performances displayed by LC^3 binders.

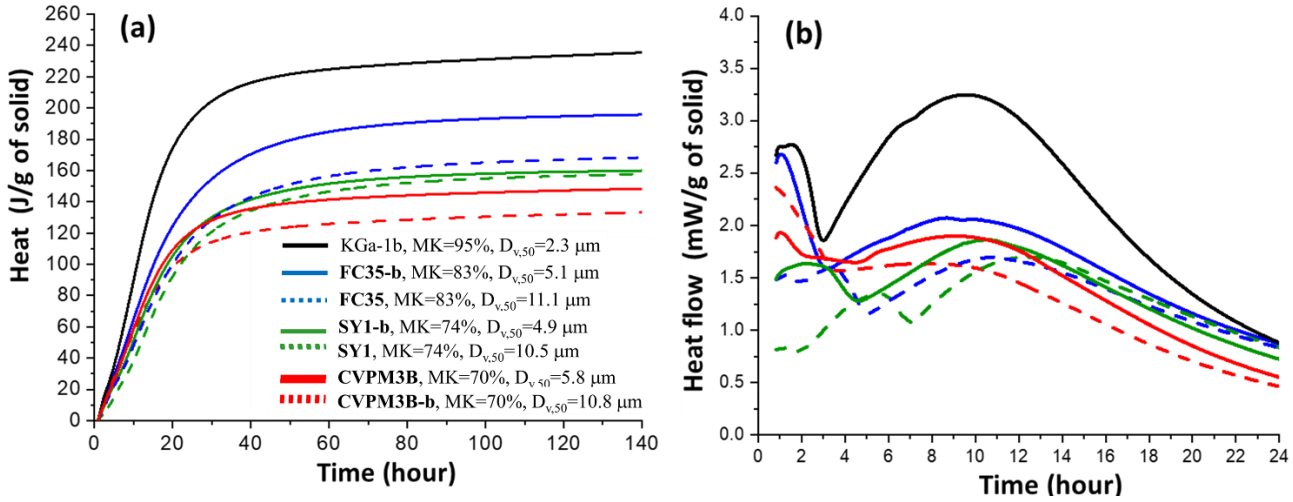

Figure 12. Calorimetric study, T=40ºC, for the calcined clays, limestone and portlandite systems. (a) Cumulative heats, up to 6 days. (b) Early age heat flows, up to 24 hours.

3.7. Mechanical strength in LC^3 binders.

The mechanical strength results for the LC^3 mortars are displayed in Figure 13 and compared to the results for the neat PC mortar. The composition of the blends was 52 wt% of PC 42.5R, 30 wt% of calcined clay (FC35, SY1 and CVPM3B with the textural properties detailed in Table 1), 15 wt% of LS and 3 wt% of additional gypsum. The mechanical strengths for the binder containing FC35 were already published [47] but they are given here for the sake of comparison. At 2 days, and as expected, the strength values of the LC^3 blends are smaller than that of the PC mortar used as a reference as the pozzolanic reactions have slower rates. At this very early age, the compressive strength values were 35(2), 20.6(2), 15.0(1) and 22.6(2) MPa for PC, FC35, SY1 and CVPM3B mortars, respectively. At 7 days of hydration, the compressive strength value for the LC^3 using the CVPM3B clay was still higher than those of FC35, SY1 due to the higher reactivity of CVPM3B clay as determined by the Frattini and calorimetry experiments. This is justified because its lower average particle size, ~5 µm, and larger disorder. Furthermore, at 28 days of hydration the compressive strength values where 58(1), 62(1), 57(1) and 58(1) MPa for neat PC and LC^3 binders with FC35, SY1 and CVPM3B calcined clays, respectively. These results prove that at 28 days, LC^3-50 binders can achieve mechanical performances even slightly better than that of neat PCs as previously reported [6,8,9]. Additionally, it also shows that at this medium hydration age, and as expected, the disorder and particle size play smaller roles and the kaolinite content is the dominant parameter.

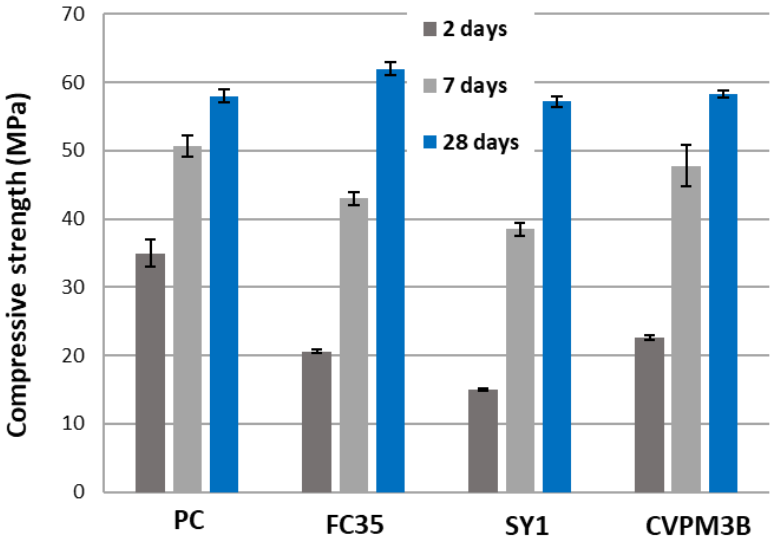

Figure 13. Mechanical strength data for neat PC and LC^3 mortars with FC35 (~11 µm), SY1 (~10 µm), CVPM3B (~6 µm) calcined clays (w/b=0.40) at 2, 7 and 28 days of hydration.

4. Conclusions

From the data reported in this work, the following four main direct conclusions can be drawn:

(i) As previously reported, to account for the overall reactivity of a calcined clay, its metakaolin content is the key feature. The estimation of this content has been carried out here by combining powder diffraction, thermal analysis and XRF.

(ii) The pozzolanic reaction rate at early ages, less than a week, strongly depends on the surface area and the local disorder of metakaolin. Consequently, the pozzolanic activities determined by Frattini are higher for calcined clays with $D_{v,50}$ values close to 5 μm than for the same clays but milled to $D_{v,50}$ values ~10 μm. This behavior is backed by the calorimetry study. At very early ages, less than one day, in addition to the metakaolin content, the local disorder is very important to justify the rate of the pozzolanic reaction. Furthermore, the compressive strengths at 2 and 7 days are higher for the binders with calcined clays with the lower particle sizes and larger disorder.

(iii) The disorder in the resulting metakaolin components has been investigated by synchrotron pair distribution function (sPDF) following the Si-O and Al-O interatomic distances. Al-O interatomic correlation position and intensity in the sPDF of the calcined kaolinitic clays could be a good descriptor to follow early age reactivity. It was found that the average Al-O distance for calcined CVPM3B was 1.95 Å that can be considered very high for the main Al(V)-O bond distances in metakaolin and this is probably a signature of the higher disorder in the original kaolinite. The higher reactivity of this calcined clay can be partly explained by the highly strained local structure.

(iv) At 28 days of hydration and 20ºC, the LC^3-50 mortar with FC35 calcined clay binder showed the highest compressive strength value, as expected, because it has the highest metakaolin content. Moreover, this work confirms that, at 28 of hydration, LC^3-50 binders can achieve mechanical performances similar or even better than those of neat PCs.

Moreover, it has been shown that in addition to the kaolinite content, the intrinsic disorder of kaolinite is important to understand the early age pozzolanic reactivities. This can be assessed by powder diffraction. A degree of freedom, for improving the mechanical strengths at early ages, is to process the calcined clays to a high finesse. However, this approach has to be cautiously exercised as it will increase the water demand that it could modify the rheological properties. Finally, there are many LC^3 studies dealing with the relationship between metakaolin content and other components and admixtures like sulfate dosage, activators and superplasticizer nature and amount. These studies should be expanded to deal with the performances of blends with similar metakaolin content and finesse, but incorporating calcined clays where the pristine kaolinite has variable intrinsic disorder.

Funding details. PID2019-104378RJ-I00 from the Spanish government and P18-RT-720 from Junta de Andalucía are acknowledged by the financial support.

Acknowledgement. CELLS-ALBA (Barcelona, Spain) is thanked for providing synchrotron beamtime at BL04-MSPD and Dr. Oriol Vallcorba for his help and support during the experiment.

Author contribution statement. I.M.R Bernal: Formal Analysis, Investigation, Writing - review & editing. M.A.G. Aranda: Conceptualization, Investigation, Writing - original draft. I. Santacruz: Investigation, Writing - review & editing. A.G. De la Torre: Investigation, Writing - review & editing. A. Cuesta: Conceptualization, Supervision, Funding acquisition, Investigation, Formal analysis, Writing - original draft.

Disclosure statement. The authors report there are no competing interests to declare.

Data availability. All synchrotron X-ray powder diffraction patterns, laboratory X-ray powder diffraction patterns, Thermal analysis, isothermal calorimetry, NMR and PSD data analyzed in this article can be freely accessed on Zenodo at https://doi.org/10.5281/zenodo.5136556, and used under the Creative Commons Attribution license.

5. References

[1] Amato I. Green cement: Concrete solutions. Nature. 2013;494:300–301.

[2] UN Environment, Scrivener KL, John VM, et al. Eco-efficient cements: Potential, economically viable solutions for a low-CO2, cement-based materials industry. Cem Concr Res. 2018;114:2–26.

[3] CEMBUREAU: The European Cement Association. https://cembureau.eu/media/kuxd32gi/cembureau-2050-roadmap_final-version_web.pdf.

[4] Alujas A, Fernández R, Quintana R, et al. Pozzolanic reactivity of low grade kaolinitic clays: Influence of calcination temperature and impact of calcination products on OPC hydration. Appl Clay Sci. 2015;108:94–101.

[5] Avet F, Snellings R, Alujas Diaz A, et al. Development of a new rapid, relevant and reliable (R3) test method to evaluate the pozzolanic reactivity of calcined kaolinitic clays. Cem Concr Res. 2016;85:1–11.

[6] Scrivener KL, Avet F, Maraghechi H, et al. Impacting factors and properties of limestone calcined clay cements (LC^3). Green Mater. 2019;7:3–14.

[7] Jaskulski R, Jóźwiak-Niedźwiedzka D, Yakymechko Y. Calcined Clay as Supplementary Cementitious Material. Materials. 2020;13:4734.

[8] Scrivener KL, Martirena F, Bishnoi S, et al. Calcined clay limestone cements (LC3). Cem. Concr. Res. Elsevier Ltd; 2018. p. 49–56.

[9] Sharma M, Bishnoi S, Martirena F, et al. Limestone calcined clay cement and concrete: A state-of-the-art review. Cem Concr Res. 2021;149:106564.

[10] Zunino F, Scrivener KL. The reaction between metakaolin and limestone and its effect in porosity refinement and mechanical properties. Cem Concr Res. 2021;140:106307.

[11] Marangu JM. Effects of sulfuric acid attack on hydrated calcined clay–limestone cement mortars. J Sustain Cem Mater. 2020;10:257–271.

[12] Vizcaíno-Andrés LM, Sánchez-Berriel S, Damas-Carrera S, et al. Industrial trial to produce a low clinker, low carbon cement. Mater Construcción. 2015;65:e045.

[13] Sui H, Hou P, Liu Y, et al. Limestone calcined clay cement: mechanical properties, crystallography, and microstructure development. J Sustain Cem Mater. 2022;published online 24 May 2022. Available from: https://www.tandfonline.com/doi/abs/10.1080/21650373.2022.2074911.

[14] Alujas-Díaz A, Almenares-Reyes RS, Arcial-Carratalá FA, et al. The Experience of Cuba TRC on the Survey of Kaolinitic Clay Deposits as Source of SCMs—Main Outcomes and Learned Lessons. In: Bishnoi S, editor. Calcined Clays Sustain Concr Proc 3rd Int Conf Calcined Clays Sustain Concr. New Delhi, India: Springer; 2020. p. 1–9.

[15] Badogiannis E, Kakali G, Tsivilis S. Metakaolin as supplementary cementitious material : Optimization of kaolin to metakaolin conversion. J Therm Anal Calorim. 2005;81:457–462.

[16] Shvarzman A, Kovler K, Grader GS, et al. The effect of dehydroxylation/amorphization degree on pozzolanic activity of kaolinite. Cem Concr Res. 2003;33:405–416.

[17] Fernandez R, Martirena F, Scrivener KL. The origin of the pozzolanic activity of calcined clay minerals: A comparison between kaolinite, illite and montmorillonite. Cem Concr Res. 2011;41:113–122.

[18] Rong Z, Jiang G, Sun W. Effects of metakaolin on mechanical and microstructural properties of ultra-high performance cement-based composites. J Sustain Cem Mater. 2018;7:296–310.

[19] Kapoor K, Singh SP, Singh B. Permeability of self-compacting concrete made with recycled concrete aggregates and metakaolin. J Sustain Cem Mater. 2017;6:293–313.

[20] Taylor-Lange SC, Lamon EL, Riding KA, et al. Calcined kaolinite-bentonite clay blends as supplementary cementitious materials. Appl Clay Sci. 2015;108:84–93.

[21] Danner T, Norden G, Justnes H. Characterisation of calcined raw clays suitable as supplementary cementitious materials. Appl Clay Sci. 2018;162:391–402.

[22] Hanein T, Thienel K-C, Zunino F, et al. Clay calcination technology: state-of-the-art review by the RILEM TC 282-CCL. Mater Struct. 2021;55:1–29.

[23] Hollanders S, Adriaens R, Skibsted J, et al. Pozzolanic reactivity of pure calcined clays. Appl Clay Sci. 2016;132–133:552–560.

[24] Egami T, Billinge SJL. Underneath the Bragg Peaks: Structural Analysis of Complex Materials. 2nd ed. Pergamon: Elsevier Science; 2012.

[25] White CE, Provis JL, Proffen T, et al. Density functional modeling of the local structure of kaolinite subjected to thermal dehydroxylation. J Phys Chem A. 2010];114:4988–4996.

[26] Lee S, Xu H. Using Complementary Methods of Synchrotron Radiation Powder Diffraction and Pair Distribution Function to Refine Crystal Structures with High Quality Parameters—A Review. Minerals. 2020;10:124.

[27] Muraleedharan MG, Asgar H, Mohammed S, et al. Elucidating Thermally Induced Structural and Chemical Transformations in Kaolinite Using Reactive Molecular Dynamics Simulations and X-ray Scattering Measurements. Chem Mater. 2020;32:651–662.

[28] White CE, Provis JL, Proffen T, et al. Combining density functional theory (DFT) and pair distribution function (PDF) analysis to solve the structure of metastable materials: The case of metakaolin. Phys Chem Chem Phys 2010;12:3239–3245.

[29] White CE, Page K, Henson NJ, et al. In situ synchrotron X-ray pair distribution function analysis of the early stages of gel formation in metakaolin-based geopolymers. Appl Clay Sci. 2013;73:17–25.

[30] Si R, Guo S, Dai Q. Influence of calcium content on the atomic structure and phase formation of alkali-activated cement binder. J Am Ceram Soc. 2019;102:1479–1494.

[31] Garg N, Skibsted J. Dissolution kinetics of calcined kaolinite and montmorillonite in alkaline conditions: Evidence for reactive Al(V) sites. J Am Ceram Soc. 2019;102:7720–7734.

[32] Skinner LB, Chae SR, Benmore CJ, et al. Nanostructure of Calcium Silicate Hydrates in Cements. Phys Rev Lett. 2010;104:195502.

[33] Morandeau AE, White CE. In situ X-ray pair distribution function analysis of accelerated carbonation of a synthetic calcium–silicate–hydrate gel. J Mater Chem A. 2015;3:8597–8605.

[34] Cuesta A, Zea-Garcia JD, Londono-Zuluaga D, et al. Multiscale understanding of tricalcium silicate hydration reactions. Sci Rep. 2018;8:8544.

[35] Cuesta A, Santacruz I, De la Torre AG, et al. Local structure and Ca/Si ratio in C-S-H gels from hydration of blends of tricalcium silicate and silica fume. Cem Concr Res. 2021;143:106405.

[36] White CE, Daemen LL, Hartl M, et al. Intrinsic differences in atomic ordering of calcium (alumino)silicate hydrates in conventional and alkali-activated cements. Cem Concr Res. 2015;67:66–73.

[37] Souza PSL, Dal Molin DCC. Viability of using calcined clays, from industrial by-products, as pozzolans of high reactivity. Cem Concr Res. 2005;35:1993–1998.

[38] Maier M, Beuntner N, Thienel KC. Mineralogical characterization and reactivity test of common clays suitable as supplementary cementitious material. Appl Clay Sci. 2021;202:105990.

[39] Ferreiro S, Canut MMC, Lund J, et al. Influence of fineness of raw clay and calcination temperature on the performance of calcined clay-limestone blended cements. Appl Clay Sci. 2019;169:81–90.

[40] Teklay A, Yin C, Rosendahl L, et al. Experimental and modeling study of flash calcination of kaolinite rich clay particles in a gas suspension calciner. Appl Clay Sci. 2015;103:10–19.

[41] Fabbri B, Gualtieri S, Leonardi C. Modifications induced by the thermal treatment of kaolin and determination of reactivity of metakaolin. Appl Clay Sci. 2013;73:2–10.

[42] Shvarzman A, Kovler K, Schamban I, et al. Influence of chemical and phase composition of

mineral admixtures on their pozzolanic activity. Adv Cem Res. 2002;14:35–41.

[43] Tironi A, Trezza MA, Scian AN, et al. Potential use of Argentine kaolinitic clays as pozzolanic material. Appl Clay Sci. 2014;101:468–476.

[44] Kakali G, Perraki T, Tsivilis S, et al. Thermal treatment of kaolin: the effect of mineralogy on the pozzolanic activity. Appl Clay Sci. 2001;20:73–80.

[45] Donatello S, Tyrer M, Cheeseman CR. Comparison of test methods to assess pozzolanic activity. Cem Concr Compos. 2010;32:121–127.

[46] Ilić BR, Mitrović AA, Miličić LR. Thermal treatment of kaolin clay to obtain metakaolin. Hem Ind. 2010;64:351–356.

[47] Bernal IMR, Shirani S, Cuesta A, et al. Phase and microstructure evolutions in LC3 binders by multi-technique approach including synchrotron microtomography. Constr Build Mater. 2021;300:124054.

[48] De la Torre AG, Bruque S, Aranda MAG. Rietveld quantitative amorphous content analysis. J Appl Crystallogr. 2001;34:196–202.

[49] Larson AC, Von Dreele RB. General structure analysis system (GSAS). Los Alamos Natl Lab Rep LAUR. 2004;748:86–748.

[50] Fauth F, Peral I, Popescu C, et al. The new Material Science Powder Diffraction beamline at ALBA Synchrotron. Powder Diffr. Cambridge University Press; Sep, 2013 p. S360–S370.

[51] Juhás P, Davis T, Farrow CL, et al. PDFgetX3: a rapid and highly automatable program for processing powder diffraction data into total scattering pair distribution functions. J Appl Crystallogr. 2013;46:560–566.

[52] Farrow CL, Juhas P, Liu JW, et al. PDFfit2 and PDFgui: computer programs for studying nanostructure in crystals. J Phys Condens Matter. 2007;19:335219.

[53] Jeong IK, Proffen T, Mohiuddin-Jacobs F, et al. Measuring Correlated Atomic Motion Using X-ray Diffraction. J Phys Chem C. 1999;103:921–924.

[54] Jeong IK, Heffner RH, Graf MJ, et al. Lattice dynamics and correlated atomic motion from the atomic pair distribution function. Phys Rev B - Condens Matter Mater Phys. 2003;67:104301.

[55] Aparicio P, Galán E, Ferrell RE. A new kaolinite order index based on XRD profile fitting. Clay Miner. 2006;41:811–817.

[56] Lothenbach B, Durdzinski P, De Weerdt K. Thermogravimetric analysis. In: K. Scrivener, R. Snellings BL, editor. A Pract Guid to Microstruct Anal Cem Mater. U.S.A: CRC Press; 2016. p. 177–211.

[57] Avet F, Scrivener KL. Investigation of the calcined kaolinite content on the hydration of Limestone Calcined Clay Cement (LC3). Cem Concr Res. 2018;107:124–135.

[58] Dollase WA. Correction of intensities of preferred orientation in powder diffractometry: application of the march model. J Appl Crystallogr. 1986;19:267–272.

[59] Fitzgerald JJ, Hamza AI, Bronnimann CE, et al. Solid-state 27Al and 29Si NMR studies of the reactivity of the aluminum-containing clay mineral kaolinite. Solid State Ionics. 1989;32–33:378–388.

[60] Rocha J, Klinowski J. 29Si and 27Al magic-angle-spinning NMR studies of the thermal transformation of kaolinite. Phys Chem Miner. 1990;17:179–186.

[61] Ruiz-Santaquiteria C, Skibsted J. Identification of reactive sites in calcined kaolinite and montmorillonite from a combination of chemical methods and solid-state nmr spectroscopy. Calcined Clays Sustain Concr Proc 2nd Int Conf Calcined Clays Sustain Concr. Springer Netherlands; 2018. p. 404–408.

[62] Zito SV, Irassar EF, Rahhal VF. Management of sanitary ware wastes as supplementary cementing materials in concretes. J Sustain Cem Mater. 2019;9:35–49.

[63] Zito S V., Cordoba GP, Irassar EF, et al. Durability of eco-friendly blended cements incorporating ceramic waste from different sources. J Sustain Cem Mater. 2022 [cited 2022

710 Aug 22]; Available from:
711 https://www.tandfonline.com/doi/abs/10.1080/21650373.2021.2010242.

712